

## Research Article

# Influence of End Structure on Electromagnetic Forces on End Winding of a 1550 MW Nuclear Generator

Chong Zeng,<sup>1</sup> Song Huang,<sup>1</sup> Yongming Yang,<sup>1</sup> and Guanghou Zhou<sup>2</sup>

<sup>1</sup>Chongqing University, Chongqing 400044, China

<sup>2</sup>Research and Test Center, Dongfang Electrical Machinery Co., Ltd., Deyang, Sichuan Province 618000, China

Correspondence should be addressed to Song Huang; [s.huang@cqu.edu.cn](mailto:s.huang@cqu.edu.cn)

Received 22 March 2017; Revised 4 August 2017; Accepted 1 October 2017; Published 29 October 2017

Academic Editor: Paolo Pennacchi

Copyright © 2017 Chong Zeng et al. This is an open access article distributed under the Creative Commons Attribution License, which permits unrestricted use, distribution, and reproduction in any medium, provided the original work is properly cited.

A 3D electromagnetic model of the end region of a 1550 MW nuclear generator is set up. The electromagnetic forces on the involute and nose parts of the end winding under a rated operation are obtained through the 3D time-step finite element method. The electromagnetic forces on different coils in the same phase are analyzed. By changing the rotor's relative length and stator coil's linear length in the 3D electromagnetic model, the electromagnetic force distributions on the end winding are obtained. The influence of each structure change on the electromagnetic force in different directions is studied in detail. Conclusions that can be helpful in decreasing the electromagnetic forces on the end winding through optimizing the end region design are presented.

## 1. Introduction

Vibrations caused by electromagnetic forces can severely damage end-winding insulations [1, 2]. Electromagnetic force increases significantly with the increase of generator capacity, thereby making large generators more vulnerable to vibration. Vibration should be decreased to ensure the security of end winding. Simply enhancing and increasing the support structures can decrease the damage of electromagnetic force but will lead to other problems, such as low utilization of materials and high manufacturing cost [3]. Optimizing the electromagnetic design for the end region can decrease electromagnetic force and vibration without extra cost. Research on the influence of end structure on the electromagnetic force on end winding can be a reference for optimization.

The accurate calculation of electromagnetic field in the end region and electromagnetic force on end winding is the basis of studies on electromagnetic force. Many studies focus on calculation.

In the early years, analytical methods were used to calculate the electromagnetic field in the end region. Methods based on the Biot-Savart law are the most popular among

them [4–6]. However, the errors in the results obtained through analytical methods are large because the end region's structure is complex. To improve the accuracy, numerical methods are utilized in the calculation. Recently, 3D finite element (FE) method has become the most popular method. Wang et al. [7] proposed full 3D models and methods for coupled electromagnetic and temperature fields in the end region of a large hydrogenerator. They discussed the effect of mesh size on the result of eddy current loss and obtained several meshing principles. Waldhart et al. [8] analyzed the influence of several common simplifications on the accuracy of the 3D FE method's results and found that the geometric details on the inner diameter, the accurate modeling of the stator winding, and the correct BH-curve of the eddy current material are essential to the electromagnetic field. Liang et al. [9] built a fine 3D geometrical model and calculated the magnetic field and eddy current loss in the end region. Wang et al. [10–14] calculated the electromagnetic field and the eddy current losses in the end region of a 330 MW turbogenerator. The influence of underexcitation [10], copper shield [11–13], and clamping plate [14] on the electromagnetic field and eddy current losses was calculated and discussed. Using the 3D

time-step FE method, Huang et al. calculated the magnetic field and the eddy current loss on the end components of a 1550 MW nuclear generator and analyzed the influences of different structural parameters on the magnetic field and the eddy current loss [15].

Relatively few studies focus on the electromagnetic force on end winding. Simplifying the end coil as straight line inductors, Richard et al. [16, 17] calculated the electromagnetic force on the end winding of a 600 MW turbogenerator using the 3D electromagnetic model of the stator end region. Senske et al. [18], Drubel et al. [19], and Grüning and Kulig [20] calculated the electromagnetic force on end winding based on the Biot-Savart law to line circuit segments. Albanese et al. [21] proposed a numerical approach based on an integral formulation to calculate the magnetic field and forces on the end winding of a large generator. Zhao et al. [22] built a 3D electromagnetic model of a 600 MW turbogenerator and calculated the electromagnetic force on the end winding using the 3D time-step FE method. Furthermore, the vibrations of the end winding were calculated and subjected to 3D FE structural analysis. None of the studies above analyzed the influence of the end structure on the electromagnetic force on end winding.

In this paper, a 3D FE model of the end region of a 1550 MW nuclear generator is set up. The electromagnetic force on the end winding at rated operation is obtained by the FE method. The rotor relative length and the stator coil linear length are set to different values in the FE model. The radial, tangential, and axial force density distributions in different parts of the end winding are presented. The influence of the two parameters on the electromagnetic force on end winding is analyzed. Conclusions that can help in decreasing the electromagnetic forces on end winding through optimal design are presented.

## 2. 3D Finite Element Model for Electromagnetic Forces Calculation

**2.1. Physical Model.** The end region of a half-speed nuclear generator is quite complex. The end part of cores and windings is 3D in structure. The end region contains three end components: copper shield, press plate, and press finger. The structure of the end region is shown in Figure 1.

**2.2. Mathematical Model for Electromagnetic Forces Calculation.** To improve computational efficiency, the following are assumed:

- (i) The distribution of current in the stator and rotor windings is uniform.
- (ii) The high-order harmonics of current and displacement current are ignored.
- (iii) The hysteresis effect is ignored. The core material is isotropic [11].
- (iv) The cross section of the solution domain of the magnetic field calculation is shown in Figure 2.

The solution domain is shown in Figure 2.  $S_1$ ,  $S_2$ , and  $S_3$  are the boundaries of the solution domain. By adopting  $A$ ,

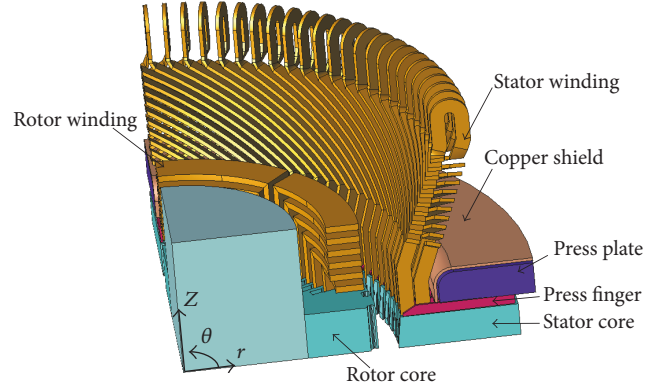


FIGURE 1: End region of a half-speed nuclear generator.

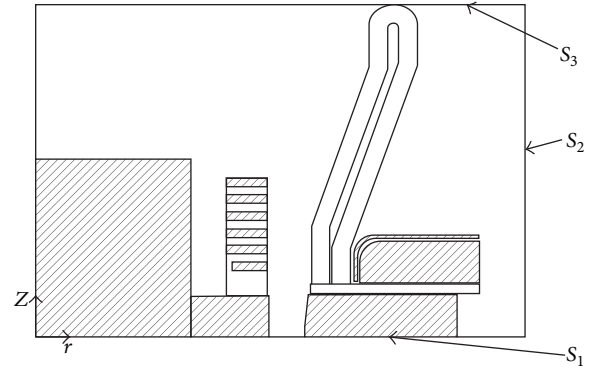


FIGURE 2: Cross section of the solution domain.

$\varphi$ - $A$  method, we can express the mathematical model of the end region as follows [23, 24]:

$$\begin{aligned} \nabla \times \left( \frac{1}{\mu} \nabla \times \mathbf{A} \right) + \sigma \frac{\partial \mathbf{A}}{\partial t} + \sigma \nabla \varphi &= \mathbf{J}_s, \\ \nabla \cdot \left( -\sigma \frac{\partial \mathbf{A}}{\partial t} - \sigma \nabla \varphi \right) &= 0, \end{aligned} \quad (1)$$

where  $\mathbf{A}$  denotes the magnetic vector potential,  $\varphi$  is the electric scalar potential,  $\sigma$  is the electrical conductivity,  $\omega$  is the angular frequency, and  $\mathbf{J}_s$  is the source current density.

The axial flux is very small in  $S_1$ . Therefore, the symmetric boundary condition, which means no flux passes across the face, is set on  $S_1$ .  $S_2$  and  $S_3$  are far from the stator and rotor cores, and their magnetic fields are weak. Therefore,  $S_2$  and  $S_3$  satisfy the first boundary condition  $\mathbf{A} = 0$ .

The stator current cannot be calculated from the above model because the solution domain only contains the end region. Thus, an additional 2D model of the generator is required. The solution domain of the 2D model is shown in Figure 3, where  $A_1$  is the inner area and  $E_1$  is the outer edge of the solution domain.

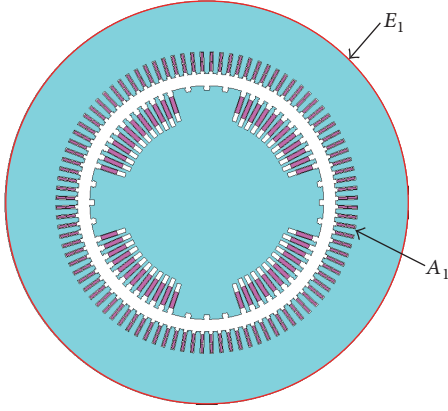


FIGURE 3: Solution domain of the 2D model.

The mathematical model can be described as follows:

$$\begin{aligned} \frac{\partial}{\partial x} \left( v \frac{\partial \mathbf{A}}{\partial x} \right) + \frac{\partial}{\partial y} \left( v \frac{\partial \mathbf{A}}{\partial y} \right) &= -\mathbf{J}_s \\ \sigma \nabla \varphi &= \mathbf{J}_s \\ &(\text{in } A_1) \\ \mathbf{A} &= 0 \quad (\text{on } E_1), \end{aligned} \quad (2)$$

$\mathbf{J}_s$  is determined by the stator current and rotor current. When a generator operates at rated condition, the rotor current is constant and the 3-phase stator currents are given as follows:

$$\begin{aligned} i_A &= I_m \sin(\omega t + \theta), \\ i_B &= I_m \sin(\omega t + \theta - 120^\circ), \\ i_C &= I_m \sin(\omega t + \theta - 240^\circ), \end{aligned} \quad (3)$$

where  $\theta$  is the angle between  $i_A$  and  $d$ -axis,  $\omega$  is the synchronous angular velocity,  $t$  is time, and  $I_m$  is the magnitude of stator phase current.

$I_m$  can be calculated with the following formula:

$$I_m = \frac{P}{(3/\sqrt{2})U \cos \varphi}, \quad (4)$$

where  $P$  is the rated power,  $U$  is the rated voltage, and  $\varphi$  is the power factor angle at rated condition.

Besides,  $\theta$  and the rotor current can be calculated by iteration.

With the magnetic field in the end region, the electromagnetic force density can be calculated as

$$\mathbf{f} = \frac{I}{S} \times \mathbf{B}, \quad (5)$$

where  $\mathbf{f}$  is the electromagnetic force density,  $I$  is the current in the coil,  $S$  is the cross-sectional area of the coil, and  $\mathbf{B}$  is the magnetic flux density.

TABLE 1: Parameters of the 1550 MW nuclear generator.

Parameters	Values
Power	1550 MW
Voltage	27 kV
Frequency	50 Hz
Number of poles	4
Current	36926.9 A
Power factor	0.9 (lagging)

TABLE 2: Iteration result of stator and rotor currents.

Parameters	Values
Rotor current	6668 A
$\theta$	$-246^\circ$

TABLE 3: Comparison between the calculated and measured value of magnetic density.

Probes	Calculated result	Measured result	Relative error
A	0.25 T	0.27 T	-7.41%
B	0.70 T	0.76 T	-7.89%
C	0.77 T	0.79 T	-2.53%

**2.3. Modeling of the Proposed Generator.** A 1550 MW nuclear generator is adopted because the electromagnetic force in a large generator is large. The basic parameters of the generator are shown in Table 1.

JMAG 12.1 is used to build the model and perform the calculation. A 3D FE model of the end region is established per the actual design of the proposed generator. The meshing of the FE model is shown in Figure 4. Using a sliding mesh, the rotation of the rotor is considered. The whole model contains 713386 elements and 129854 nodes.

A 2D FE model of the generator is set up with ANSYS Maxwell 16.1. The stator and rotor currents are obtained by iteration at a rated condition. The result is shown in Table 2.

**2.4. Validation of the Model.** The experiment is performed on an 1150 MW nuclear generator because the 1550 MW nuclear generator is not available for the experiment. The FE model of the 1150 MW generator is built on the same principles, and the structure of the 1150 MW nuclear generator is almost the same as but smaller than that of the 1550 MW generator. Therefore, the relative errors of the two FE models have a similar order. Three probes are set as shown in Figure 5. The comparison of the magnetic flux densities at no-load operation between the computational and experimental results is shown in Table 3. Table 3 shows that the calculation method is reasonable and the relative error of the calculated result is within 10%.

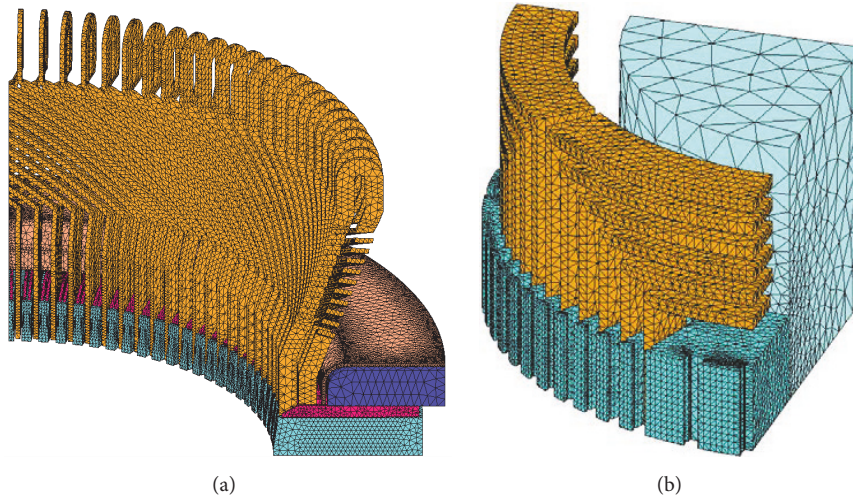


FIGURE 4: FE model mesh of the proposed generator end region. (a) Stator. (b) Rotor.

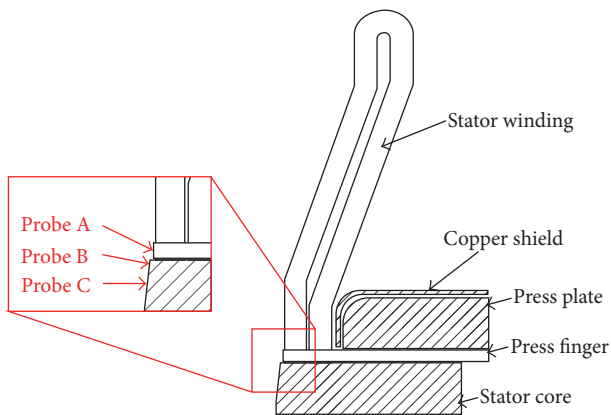


FIGURE 5: Distribution of the test points.

### 3. Electromagnetic Forces on End Winding

We should analyze only the electromagnetic force on one winding phase because the generator and the electromagnetic force on each winding phase are symmetric. The electromagnetic forces on phase A are analyzed in this paper. In the proposed generator, a winding phase has eight coils. The eight coils are numbered as shown in Figure 6. An end coil can be divided into several parts and the definition of these parts is shown in Figure 7.

The magnetic fields on different coils in the same phase are different. Therefore, the electromagnetic forces on different coils are also different, as shown in Figure 8. The forces on the involute parts change significantly. Generally, the forces on the upper involute parts increase with the coil number. Conversely, the forces on the lower involute parts decrease with the coil number. The upper involute part suffers the largest force among all the involute parts. The

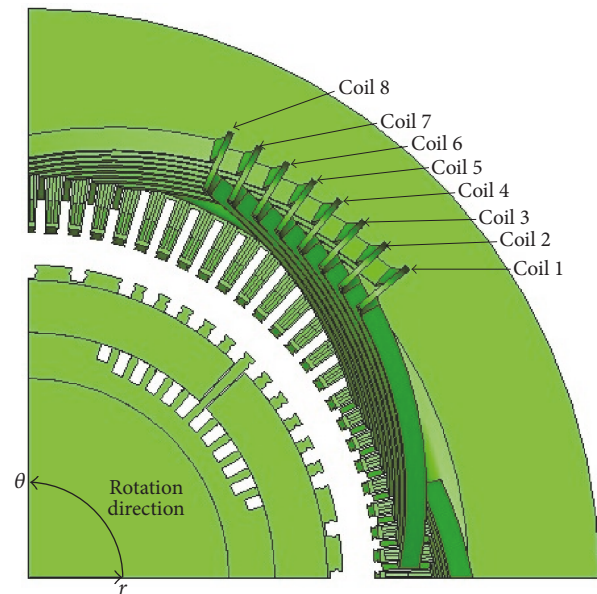


FIGURE 6: Numbering of phase A coils.

electromagnetic forces on the nose parts are smaller than the forces on the involute parts, and they change slightly.

### 4. Parametric Study on Electromagnetic Forces on End Winding

Although the force on the nose part is smaller than that on the involute part, the vibration on the nose part is even larger than that on the involute part because of the weak constraint [22]. The influences of the end structure parameters on the electromagnetic force on the involute part and the force on

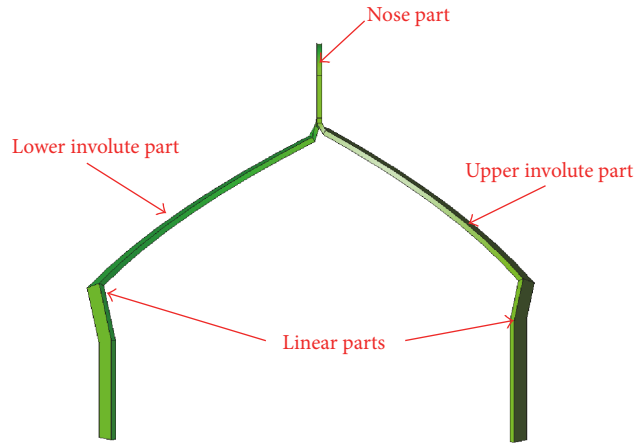


FIGURE 7: Definition of the parts of the end coil.

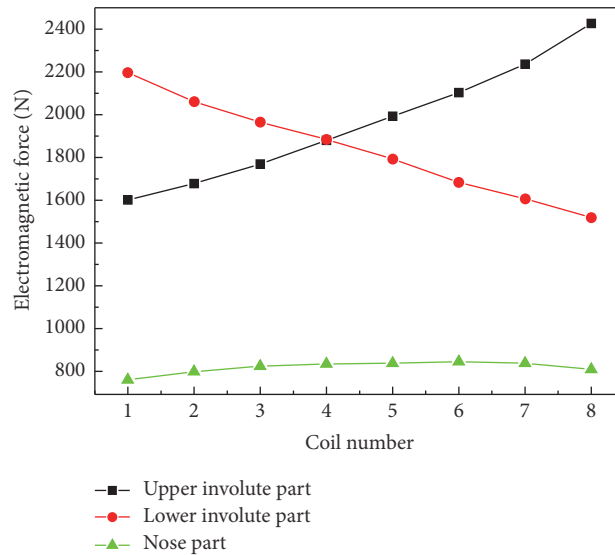


FIGURE 8: Electromagnetic forces on different coils of phase A.

the nose part are analyzed in this section. To simplify the analysis, only the forces on coil 8 are studied in detail. Only the upper involute part and the nose are analyzed because the constraints of the upper and lower involute parts are almost the same.

**4.1. Influence of the Relative Length of Rotor.** Rotor relative length ( $l_r$ ) is defined as shown in Figure 9. The lengths of the rotor core and winding change with  $l_r$ . When the rotor core is longer than the stator core,  $l_r$  is positive. Conversely, when the rotor core is shorter than stator core,  $l_r$  is negative. To study the influence of the rotor relative length on electromagnetic force,  $l_r$  is set to  $-75$ ,  $0$ , and  $75$  mm in the FE model.

The electromagnetic force distribution on the involute part at  $0.039$  s is shown in Figure 10. Most of the forces reach

their maximums at the same time because the current in the coil reaches the maximum at  $0.039$  s. Figure 10 shows that radial force is the largest and increases with  $l_r$ . The tangential and axial forces are smaller than the radial force and decrease with the increase of  $l_r$ . For the three components, the changes are more significant at the side close to the linear part (the right side of each involute part in Figure 10). When  $l_r$  varies from  $-75$  mm to  $+75$  mm, the maximum of the electromagnetic force density varies from  $2.3 \times 10^6$  N/m<sup>3</sup> to  $2.6 \times 10^6$  N/m<sup>3</sup>,  $1.2 \times 10^6$  N/m<sup>3</sup> to  $1.0 \times 10^6$  N/m<sup>3</sup>, and  $1.8 \times 10^6$  N/m<sup>3</sup> to  $1.4 \times 10^6$  N/m<sup>3</sup> in the radial, tangential, and axial directions, respectively.

Figure 11 shows the maximum electromagnetic forces on the involute part with different  $l_r$ . Figure 11 shows that the radial force is relatively larger than the tangential and axial

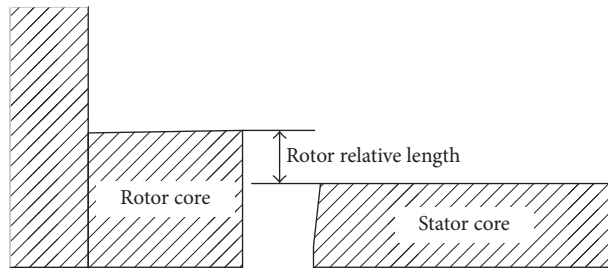


FIGURE 9: Definition of rotor relative length.

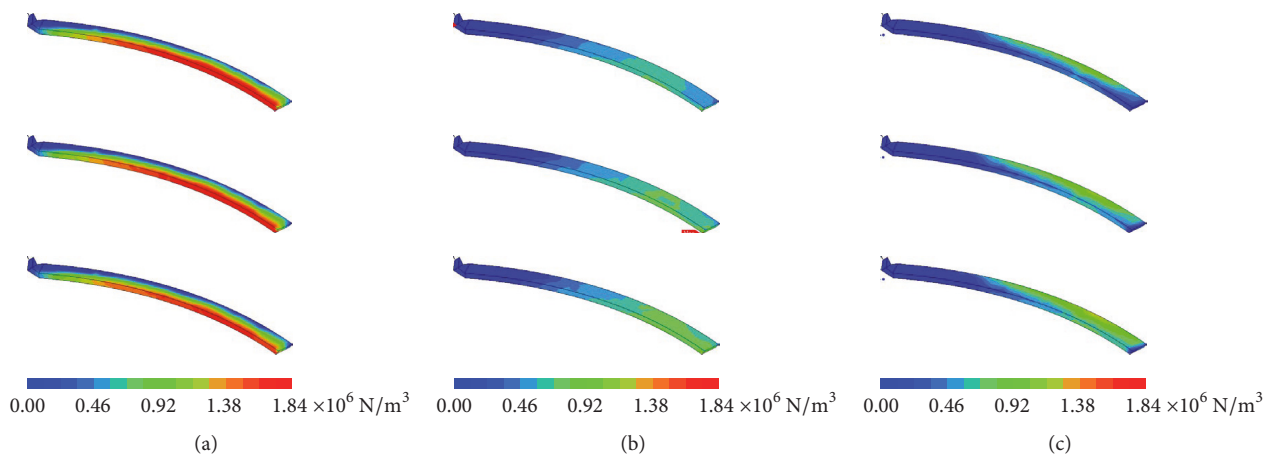


FIGURE 10: Electromagnetic force density distribution on the involute part at 0.039 s, when  $l_r = -75$  mm (bottom),  $l_r = 0$  mm (middle), and  $l_r = 75$  mm (top). (a) Radial component. (b) Tangential component. (c) Axial component.

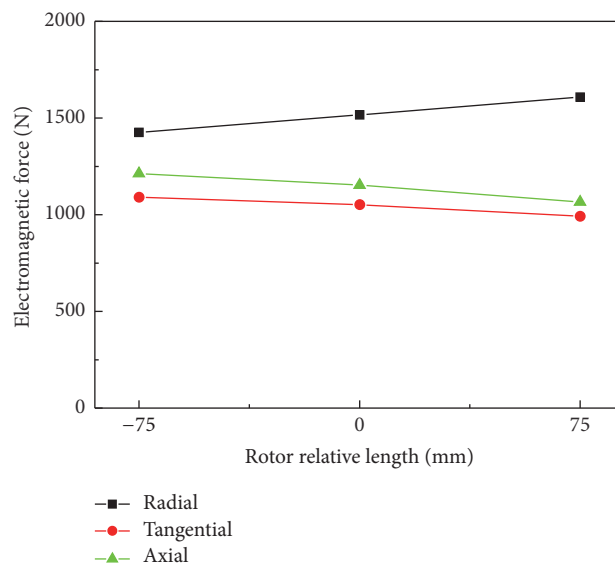


FIGURE 11: Electromagnetic forces on the involute part with different rotor relative lengths.

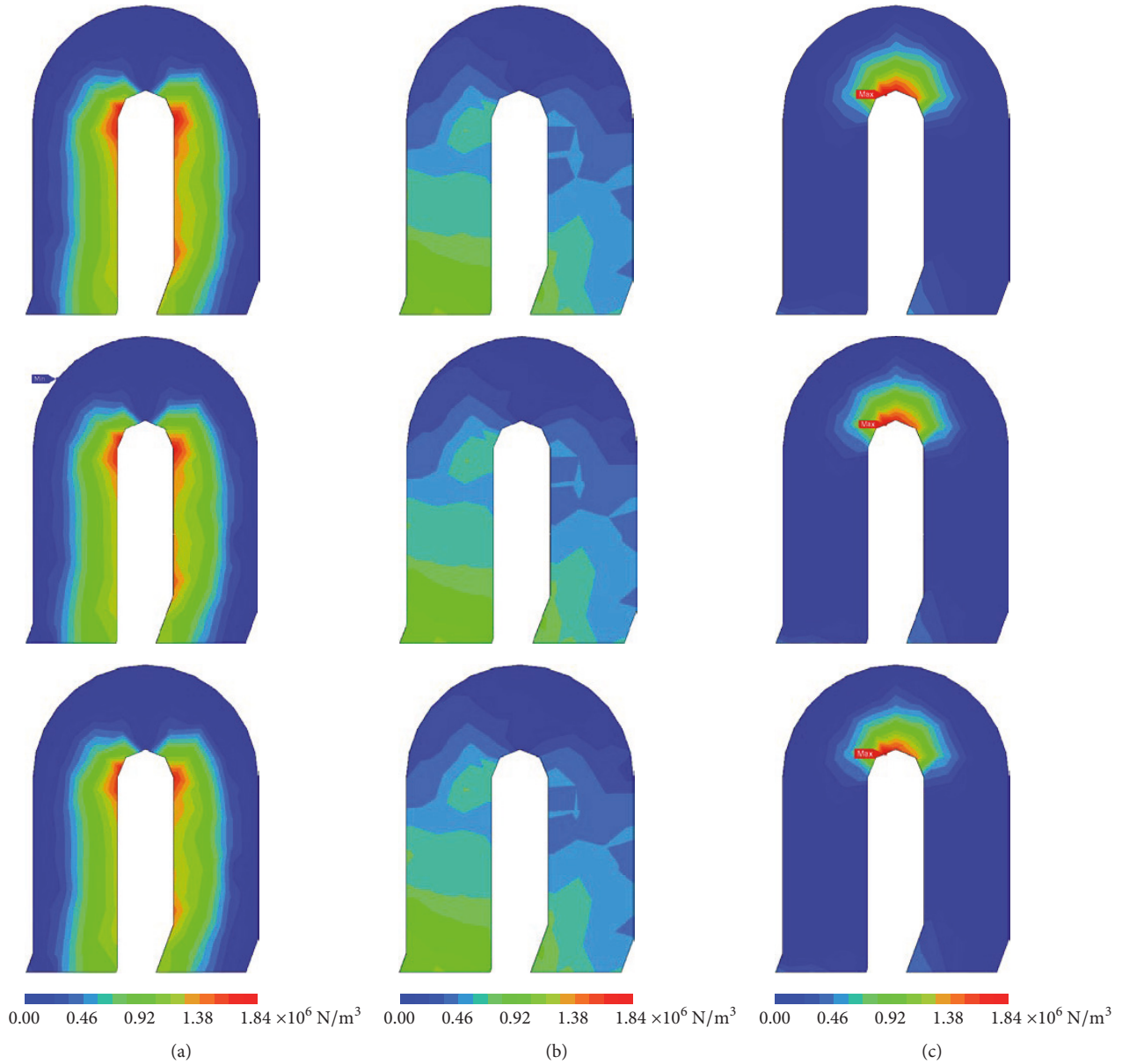


FIGURE 12: Electromagnetic force density magnitude distribution on the nose part at 0.039 s, when  $l_r = -75$  mm (bottom),  $l_r = 0$  mm (middle), and  $l_r = 75$  mm (top). (a) Radial component. (b) Tangential component. (c) Axial component.

forces. When  $l_r$  increases from  $-75$  mm to  $+75$  mm, the radial force increases by 13% while the tangential and axial forces decrease by 9% and 12%, respectively.

The electromagnetic force distribution on the nose part is shown in Figure 12. The magnitude of the force density is used to show the change in force strength because the direction of the force density changes to the opposite direction of the axis on some areas of the nose part. Figure 12 shows that the radial and axial force densities increase with  $l_r$ . The radial force change mainly appears at the inner side of the nose part, and the axial force change mainly appears at the inner side of the top section of the nose part. When  $l_r$  varies from  $-75$  mm to

$+75$  mm, the maximum of the electromagnetic force density varies from  $1.9 \times 10^6$  N/m<sup>3</sup> to  $2.0 \times 10^6$  N/m<sup>3</sup>,  $1.0 \times 10^6$  N/m<sup>3</sup> to  $1.0 \times 10^6$  N/m<sup>3</sup>, and  $2.1 \times 10^6$  N/m<sup>3</sup> to  $2.2 \times 10^6$  N/m<sup>3</sup> in the radial, tangential, and axial directions, respectively.

The maximum electromagnetic forces on the nose part with different rotor relative lengths are shown in Figure 13. The radial force is smaller than the tangential and axial forces because the direction of the radial force on both sides of the nose part are opposite and almost offset each other. When  $l_r$  varies from  $-75$  mm to  $+75$  mm, the radial and axial forces increase by 8% and 23%, respectively, while the tangential force almost stays constant.

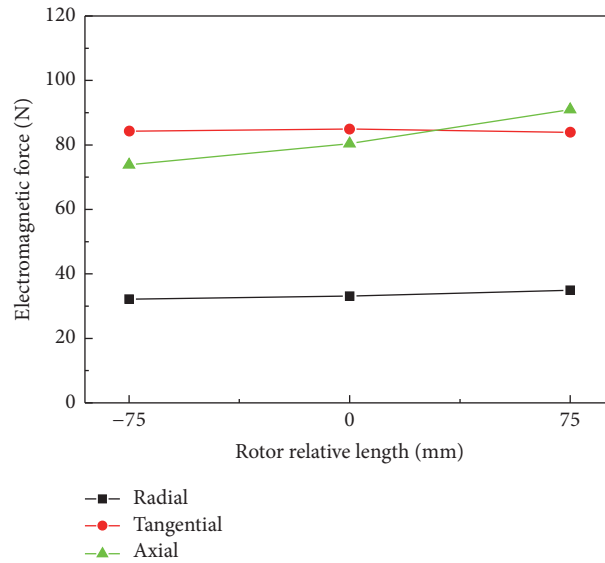


FIGURE 13: Electromagnetic forces on the nose part with different rotor relative lengths.

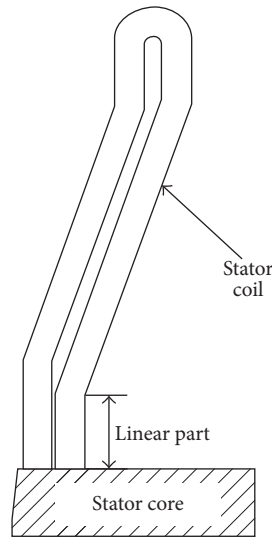


FIGURE 14: Definition of stator coil linear length.

For large generators, the radial vibration of end winding is the most serious [22]. A relatively short rotor can be adopted to reduce the radial vibration from the source. Both the electromagnetic force on the involute and nose parts are smaller with a relatively short rotor. The axial force on the nose part (especially on the top of the inner side) also decreases. However, the tangential and axial forces on the involute part (especially on the region close to the linear part of the end coil) increase at the same time.

**4.2. Influence of Stator Coil Linear Length.** The stator coil linear length ( $l_{sc}$ ) is defined in Figure 14 as the length of

the lower linear part beyond the stator core. To study the influence of  $l_{sc}$  on electromagnetic force,  $l_{sc}$  is set to 221, 271, 321, 371, and 421 mm in the FE model.

The electromagnetic force density distributions on the involute part at 0.039 s with different stator coil linear lengths are shown in Figure 15. Figure 15 shows that the radial force decreases slightly with the increasing  $l_{sc}$ , and the maximum of the radial electromagnetic force is reduced to  $2.3 \times 10^6 \text{ N/m}^3$  when  $l_{sc}$  is 421 mm from  $2.7 \times 10^6 \text{ N/m}^3$  when  $l_{sc}$  is 221 mm. The tangential and axial forces increase significantly with  $l_{sc}$ . The maximums of the tangential and axial forces increase to  $1.1 \times 10^6 \text{ N/m}^3$  and  $1.8 \times 10^6 \text{ N/m}^3$ , respectively, when  $l_{sc}$  is

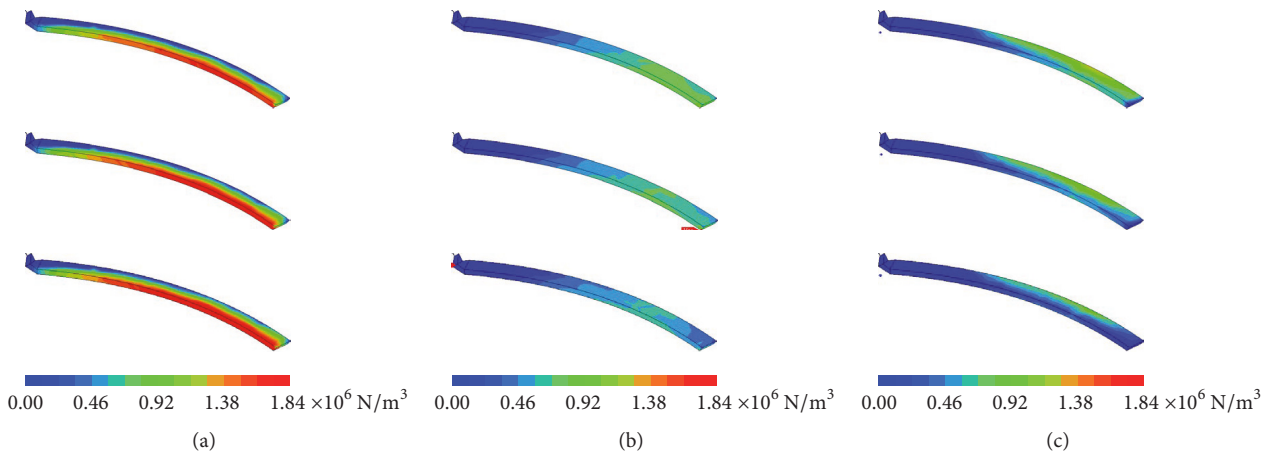


FIGURE 15: Electromagnetic force density distribution on the involute part at 0.039 s, when  $l_{sc} = 221$  mm (bottom),  $l_{sc} = 321$  mm (middle), and  $l_{sc} = 421$  mm (top). (a) Radial component. (b) Tangential component. (c) Axial component.

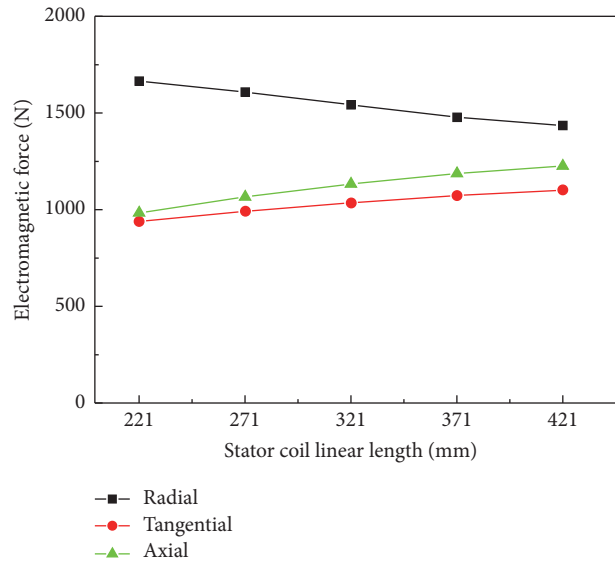


FIGURE 16: Electromagnetic forces on the involute part with different stator coil linear length.

421 mm from  $0.9 \times 10^6$  and  $1.3 \times 10^6$  N/m<sup>3</sup>, respectively, when  $l_{sc}$  is 221 mm.

Figure 16 shows the maximum electromagnetic forces on the involute part with different  $l_{sc}$ . Figure 16 shows that the radial force is relatively larger than the tangential and axial forces. When  $l_{sc}$  increases from 221 mm to 421 mm, the radial force decreases by 14% while the tangential and axial forces increase by 17% and 24%, respectively.

The distribution of the electromagnetic force density magnitude on the nose part with different  $l_{sc}$  is shown in Figure 17. The influence of the stator coil linear length on electromagnetic force on the nose part is small. Generally, the radial force decreases with the increase of the stator

coil's linear length. Conversely, the tangential force increases with the stator coil's linear length. The axial force is constant against the changes in stator coil linear length.

Figure 18 shows the maximum electromagnetic forces on the nose part with different  $l_{sc}$ . When  $l_{sc}$  increases from 221 mm to 421 mm, the radial and axial forces decrease by 9% and 17%, respectively, while the tangential force remains almost constant.

To reduce the radial vibration on end winding, a relatively large stator coil linear length can be adopted. Consequently, the radial force on the involute and nose parts and the axial force on the nose part will decrease. In contrast, the tangential and axial forces on the involute part increase.

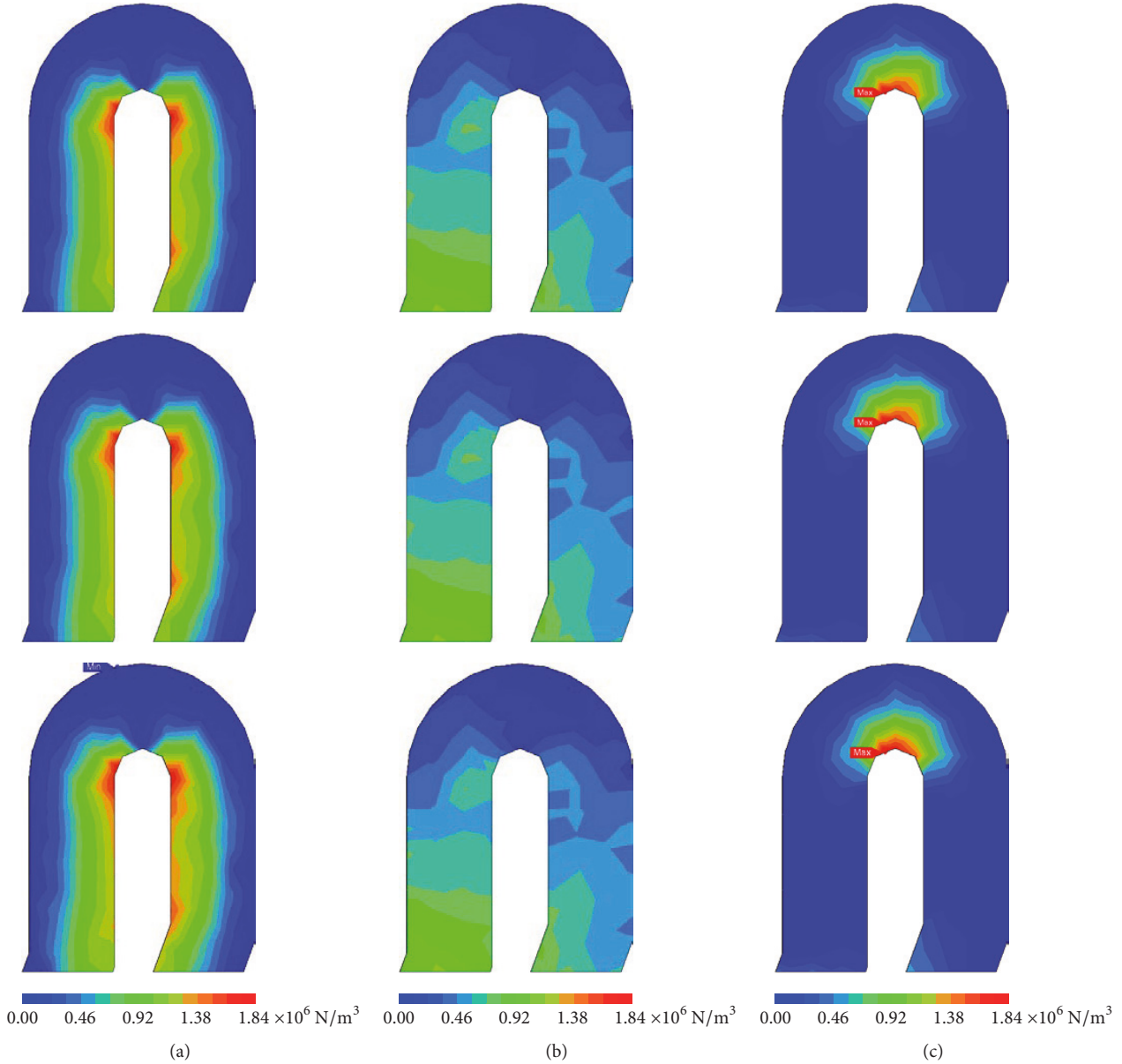


FIGURE 17: Electromagnetic force density magnitude distribution on the nose part at 0.039 s, when  $l_{sc} = 221$  mm (bottom),  $l_{sc} = 321$  mm (middle), and  $l_{sc} = 421$  mm (top). (a) Radial component. (b) Tangential component. (c) Axial component.

## 5. Conclusions

In this paper, a 3D FE model of the end region of a 1550 MW nuclear generator is set up. The electromagnetic force on the stator end winding at a rated operation is calculated. The electromagnetic forces on different coils in the same phase are presented. By changing the rotor relative length and stator coil linear length in the FE model, the influence of these parameters on electromagnetic force is analyzed in detail. The following conclusions are drawn:

- (1) The electromagnetic force on the involute part varies in different coils at the same phase and the upper involute part of the last coil in the rotation direction

suffers the largest force. The electromagnetic force on the nose part is smaller than that on the involute part and changes slightly in different coils.

- (2) Decreasing the rotor relative length decreases the radial forces on the involute and nose parts. However, decreasing the rotor relative length increases the tangential and axial forces on the involute parts.
- (3) The stator coil linear length can be increased to decrease the radial forces on the end winding. The radial force on the involute and nose parts decreases significantly but the tangential and axial forces on the involute parts simultaneously increase.

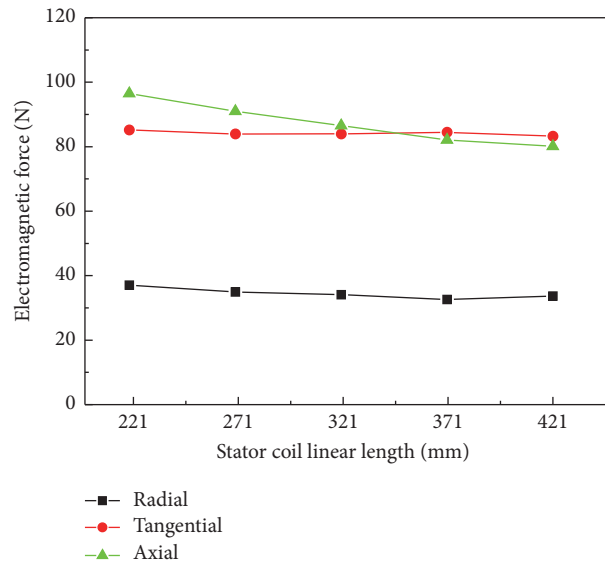


FIGURE 18: Electromagnetic forces on the nose part with different stator coil linear lengths.

## Conflicts of Interest

The authors declare that they have no conflicts of interest.

## Acknowledgments

The work is financially supported by the project supported by the National Natural Science Foundation of China (Grant no. 51477015).

## References

- [1] D. Shally, M. Farrell, and K. Sullivan, "Generator end winding vibration monitoring," in *Proceedings of the 43rd International Universities Power Engineering Conference (UPEC '08)*, pp. 1–5, Padova, Italy, September 2008.
- [2] S. Wan, C. Zhan, X. Yao, Y. Deng, and G. Zhou, "Investigation on electromagnetic forces and experimental vibration characteristics of stator end windings in generator," *Transactions of the Canadian Society for Mechanical Engineering*, vol. 38, no. 3, pp. 331–345, 2014.
- [3] H. Yuda, Q. Jiajun, and Q. Guanghui, "Calculation of electromagnetic force and vibration on end winding of turbo generators," in *Proceedings of the 10th National Academic Conference of Structure Engineering*, Nanjing, China, 2001 (Chinese).
- [4] J. F. Calvert, "Forces in turbine generator stator windings," *Transactions of the American Institute of Electrical Engineers*, vol. 50, no. 1, pp. 178–194, 1931.
- [5] D. Harrington, "Forces in machine end windings," *Electrical Engineering*, vol. 72, no. 2, pp. 153–153, 1953.
- [6] M. Ohtaguro, K. Yagiuchi, and H. Yamaguchi, "Mechanical behavior of stator endwindings," *IEEE Transactions on Power Apparatus and Systems*, vol. 99, no. 3, pp. 1181–1185, 1980.
- [7] H. Wang, R. Zong, L. Liu, and S. Yang, "Full 3D eddy current and temperature field analysis of large hydro-generators in different operating conditions," in *Proceedings of the 17th International Conference on Electrical Machines and Systems (ICEMS '14)*, pp. 3599–3603, Hangzhou, China, October 2014.
- [8] F. J. Waldhart, J. P. Bacher, and G. Maier, "Modeling eddy current losses in the clamping plate of large synchronous generators using the finite element method," in *Proceedings of the 21st International Symposium on Power Electronics, Electrical Drives, Automation and Motion (SPEEDAM '12)*, pp. 1468–1473, Sorrento, Italy, June 2012.
- [9] Y.-P. Liang, H.-H. Wang, J.-T. Zhang, and J. Liu, "Research of end fields and eddy current losses for air-cooling steam-turbogenerator," *Journal of Electric Machines and Control*, vol. 14, no. 1, pp. 29–34, 2010 (Chinese).
- [10] L. Wang, W. Li, F. Huo, S. Zhang, and C. Guan, "Influence of underexcitation operation on electromagnetic loss in the end metal parts and stator step packets of a turbogenerator," *IEEE Transactions on Energy Conversion*, vol. 29, no. 3, pp. 748–757, 2014.
- [11] H. Feiyang, L. Weili, W. Likun, G. Chunwei, Z. Yihuang, and L. Yong, "Influence of copper screen thickness on three-dimensional electromagnetic field and eddy current losses of metal parts in end region of large water-hydrogen-hydrogen-cooled turbogenerator," *IEEE Transactions on Industrial Electronics*, vol. 60, no. 7, pp. 2595–2601, 2013.
- [12] H. Feiyang, H. Jichao, L. Weili et al., "Influence of copper shield structure on 3-D electromagnetic field, fluid and temperature fields in end region of large turbogenerator," *IEEE Transactions on Energy Conversion*, vol. 28, no. 4, pp. 832–840, 2013.
- [13] L. Wang, F. Huo, W. Li et al., "Influence of metal screen materials on 3-D electromagnetic field and eddy current loss in the end region of turbogenerator," *IEEE Transactions on Magnetics*, vol. 49, no. 2, pp. 939–945, 2013.
- [14] W. Likun, L. Weili, X. Yi, and G. Chunwei, "Influence of clamping plate permeability and metal screen structures on three-dimensional magnetic field and eddy current loss in end region of a turbo-generator by numerical analysis," *Journal of Applied Physics*, vol. 114, no. 19, Article ID 193904, 2013.
- [15] S. Huang, C. Zeng, Y. Yang, and G. Zhou, "Influence of the end structure on the leakage magnetic field and eddy current loss in a 1,550 MW nuclear generator," *Proceedings of the Chinese Society of Electrical Engineering*, vol. 36, pp. 200–205, 2016.

- [16] N. Richard, F. Duffeau, A. C. Leger, and N. Szylowicz, "Computation of forces and stresses on generator end windings using a 3d finite element method," *IEEE Transactions on Magnetism*, vol. 32, no. 3, pp. 1689–1692, 1996.
- [17] N. Richard, "Calculation of electromagnetic forces on large generator end-windings under fault conditions using a three-dimensional finite element method," *Mathematics and Computers in Simulation*, vol. 46, no. 3-4, pp. 257–263, 1998.
- [18] K. Senske, S. Kulig, J. Kauhoff, and D. Wunsch, "Vibrational behaviour of the turbogenerator stator end winding in case of electrical failures," in *Proceedings of the Conférence Internationale des Grands Réseaux Electriques*, pp. 1–12, Yokohama, Japan, October 1997.
- [19] O. Drubel, S. Kulig, and K. Senske, "End winding deformations in different turbo generators during 3-phase short circuit and full load operation," *Electrical Engineering*, vol. 82, no. 3, pp. 145–152, 2000.
- [20] A. Grüning and S. Kulig, "Electromagnetic forces and mechanical oscillations of the stator end winding of turbogenerators," in *Recent Developments of Electrical Drives*, pp. 115–126, Springer, The Netherlands, 2006.
- [21] R. Albanese, F. Calvano, G. Dal Mut et al., "Coupled three dimensional numerical calculation of forces and stresses on the end windings of large turbo generators via integral formulation," *IEEE Transactions on Magnetism*, vol. 48, no. 2, pp. 875–878, 2012.
- [22] Y. Zhao, B. Yan, C. Zeng, S. Huang, C. Chen, and J. Deng, "Dynamic response analysis of large turbogenerator stator end structure under electromagnetic forces," *Transactions of China Electrotechnical Society*, vol. 31, no. 5, pp. 199–206, 2016.
- [23] J. Cheaytani, A. Benabou, A. Tounzi, and M. Dessoude, "Stray load losses analysis of cage induction motor using 3-D finite element method with external circuit coupling," in *Proceedings of the 17th Biennial IEEE Conference on Electromagnetic Field Computation (CEFC '16)*, Miami, Fla, USA, November 2016.
- [24] K. Yamazaki, S. Kuramochi, N. Fukushima, S. Yamada, and S. Tada, "Characteristics analysis of large high speed induction motors using 3-D finite element method," *IEEE Transactions on Magnetism*, vol. 48, no. 2, pp. 995–998, 2012.



**Hindawi**

Submit your manuscripts at  
<https://www.hindawi.com>

